Astron. Astrophys. 330, 327–335 (1998)

ASTRONOMY
AND
ASTROPHYSICS

The physical structure of the Herbig Haro object HH 29⋆

C.V.M. Fridlund[1], **R. Liseau**[2], **and E. Gullbring**[2,3]

[1] Astrophysics Division, Space Science Department of ESA, ESTEC, 2200 AG Noordwijk, The Netherlands (mfridlun@estec.esa.nl)
[2] Stockholm Observatory, S-133 36 Saltsjöbaden, Sweden (rene@astro.su.se and erik@astro.su.se)
[3] Harvard/Smithsonian Center for Astrophysics, 60 Garden Street, Cambridge, MA 02158, USA

Received 20 May 1997 / Accepted 15 September 1997

Abstract. We have obtained Echelle spectra covering a number of important shock diagnostic emission lines, mapping out the full extent of the Herbig-Haro object HH 29. Through this, the velocity field, the level of excitation and the electron density have all been determined with a spatial resolution of $1'' - 2''$ and a spectral resolution of $10\,\mathrm{km\,s^{-1}} - 20\,\mathrm{km\,s^{-1}}$ respectively. Our observations of shock diagnostic lines allow us to produce an empirical 3D description (velocity is the third dimension) of F(Hα), the level of excitation and the electron density. Our results indicate that HH 29 is among the Herbig-Haro objects with the highest level of excitation. We derive electron densities of between a few thousand $\mathrm{cm^{-3}}$ and 10^4 $\mathrm{cm^{-3}}$ in 'clumps' interspersed in an 'inter-clump medium' of density $\sim 300\,\mathrm{cm^{-3}}$. The spatial scale of the clumps is $\lesssim 2''$, and the velocity dispersion of individual clumps is on the order of 30km $\mathrm{s^{-1}}$ – 50 km $\mathrm{s^{-1}}$, implying that the 'knotty' structure obvious in high spatial resolution images also exist in 3 dimensions. Based on the morphological and spectroscopical data, HH 29 appears to consist of a number of HH-knots where the shock is located on the side of the object oriented towards the originating source in some and on the opposite side in others. We find that HH 29 is best explained as an aggregate of clumps interacting with ambient material on the side *away* from the originating source, and also being shocked by a faster wind on the side *towards* the originating source.

Key words: stars formation – ISM: jets and outflows– ISM: individual objects: HH 29

1. Introduction

Herbig-Haro objects (HH) are emission line objects, observed from radio to UV wavelengths, and found in the immediate vicinity of young stellar objects (YSO). Present theoretical understanding interprets these objects as the cooling radiation emanating from shocks formed when out-flowing gas from the vicinity of the YSO interacts with either itself or the ambient medium. HH objects can, based on their spectra, broadly be divided into high excitation- and low excitation objects. Four types of models have been invoked in order to explain the HH phenomenon: The 'Shocked cloudlet' model (Schwartz, 1978), where a wind emanating from the YSO impacts and shocks a denser cloudlet in the ambient medium; The 'interstellar bullet' scenario (Norman & Silk, 1979), where a small relatively denser cloud is ejected from the vicinity of the YSO and the shock appears as it plows through the ambient medium; The cavity model (Canto, 1980), where shocks are caused by an expanding wind, interacting with the walls of a cavity evacuated by the wind itself. The fourth type is the jet/working surface scenario (Königl, 1982), in which a well collimated atomic jet escapes from the YSO with a very high velocity and shocks at its end ('working surface'), as well as experiencing crossing shocks along the way (e.g. Raga, 1995). Many but not all HH objects appear to be best modeled as the consequence of a jet (e.g. Böhm, 1995), and it could thus be that several of these mechanisms take place in nature.

One case, where this could be true, is in the molecular outflow/HH complex in the L1551 cloud. The originating source of the outflow is designated IRS5, and identified as a low mass YSO by Fridlund et al. (1980). From IRS5 a short ($20''$) well collimated jet emanates (Mundt & Fried, 1983; Fridlund & Liseau, 1994). This jet falls well along the major axis of a large bipolar molecular outflow, which extends for several arc min in opposite directions from IRS5. The molecular source has been well studied. The geometry of the outflow has been modeled as evacuated molecular shells, filled with a faster ($\sim 150\,\mathrm{km\,s^{-1}}$ versus $\lesssim 50$ km $\mathrm{s^{-1}}$ for the molecular component) HI wind (see Staude & Elsässer, 1993 and references theirin). Within the approaching lobe a large number of HH objects is found scattered. Two of these HH objects – HH 28 & HH 29 – have had their proper motion vectors determined (Cudworth & Herbig, 1979). Their tangential velocity is ~ 150 km $\mathrm{s^{-1}}$, and the origin of the vectors when extrapolated, is found near IRS5. The distance to L1551 is only ~ 140 pc (Elias, 1978) allowing the resolution of quite small spatial elements.

Send offprint requests to: C.V.M. Fridlund

⋆ Based on observations collected at the European Southern Observatory, La Silla, Chile

Table 1. Ions observed in HH 29a

Ion	Rest wavelength (Å)	Line width [1] (km s^{-1})
$[OII]$	3727/29[2]	–
$H\beta$	4861[2]	–
$[OIII]$	5007[2]	–
$[OI]$	6300.22	210
$[OI]$	6363.81	167
$[NII]$	6548.1	197
$H\alpha$	6562.817	240
$[NII]$	6583.6	230
$[SII]$	6716.42	199
$[SII]$	6730.78	193
$[FeII]$	7155.14	163
$[CaII]$	7291.46	157
$[OII]$	7319.4	–
$[CaII]$	7323.88	–
$[OII]$	7329.9	–

[1] Maximum FWZI$_M$ line width as defined in Sect. 3.1 for HH 29a
[2] Data from Fridlund, Liseau, Perryman (1993)

Fridlund, Liseau and Perryman (1993, hereafter FLP) performed imaging spectrophotometry of HH 29. They found evidence of high excitation and thus of a strong shock localized at the brightest portion of the object (which was designated HH 29a – $\sim$ 20% of the line flux emanates from this object). The high excitation nature of HH 29a is further substantiated by the IUE results of Cameron & Liseau (1990) and by Liseau et al. (1996 - hereafter LHFC). These authors also find evidence for significant flux variation on time scales of $\lesssim$6 months. Estimates of the extinction (A$_V$ $\sim$ 3 – 5 magnitudes) indicate that the HH 29 object is located within the molecular cavity, probably interacting with the cavity walls. HH 29a only makes up 4 % of the total area of HH 29 and the rest of the object also has a decidedly 'clumpy' structure, very reminiscent of HH1-2 and HH32 (e.g. Hartigan et al. 1987 – hereafter HRH; Choe, Böhm & Solf, 1985).

In view of the large body of available data, as well as the above mentioned proximity which allows both the resolution of small spatial elements and that of detecting faint spectral features at high velocity resolution, we have decided to attempt the mapping of the radial velocity field of HH 29, at the highest possible spatial and spectral resolutions. We also strived to observe as many shock diagnostic spectral lines as possible. Our ultimate goal is to use the current results together with our previously published data (FLP, LHFC) to characterize physical parameters and to build a 3-D empirical model which can be compared with available (bow-) shock models. We also aim at confirming the size scale and densities of the 'mini-clumps' by analyzing the characteristics of the radiation field with respect to the velocities. In this paper we concentrate on the Hα and the [SII] data which provides information about the electron density, n$_e$, the level of excitation and the 'clumpiness' of the object in 3 dimensions through a study of how the flux in Hα and the above mentioned quantities vary as a function of velocity and of the spatial coordinates.

2. Observations and data reductions

The observations where carried out on the nights of 12 – 14 December, 1992, using the ESO 3.5m NTT telescope. We used the red arm of the EMMI (ESO Multi-Mode Instrument) in its Echelle mode using grating No. 10 with grism No. 6 as a cross-disperser. A 20″ decker was mounted in order to limit the length of the slit, and the slit width was set to 2″. This slit width was selected as a compromise, in order to cover as much as possible of the object in the allotted time. This combination resulted in a mean resolution of $\Delta\lambda/\lambda \sim 28000$ in the wavelength interval of 6200Å to 8100Å, equivalent to a velocity resolution of 10.7 km s^{-1} at the wavelength of Hα. The detector utilized was ESO CCD No. 18, with 1060 $\times$ 1040 19μm pixels. The image scale translates as 0.44″ pixel^{-1} and 4.5 km s^{-1} pixel^{-1} respectively.

On the first night we obtained spectra at 3 positions, with the slit in an E-W orientation. The exposure time for these spectra was 3$\times$0.5 hours per position. The first spectrum was centered on the intensity maximum of HH 29a, and the two following spectra were obtained by moving the telescope 2″ due north and 2″ due south of this position. The seeing was measured as 0.″7. On the second night we obtained 5 spectra with the slit in a N-S orientation. The integration time for these were 2$\times$0.5 hours per position. The seeing was worse than on the previous night – 1.″5 – but still matched to the slit width utilized. We centered the first exposure 1″W of the intensity maximum in HH 29a and each subsequent spectrum was obtained by moving the telescope 2″ W from the previous position. The final spectrum (No. 8) was obtained by centering the slit on the small knot/filament, towards the east of HH 29 and exposing for 0.5 hour at this position. In Fig. 1, we show two Hα-images of HH 29, with the slit positions superposed.

In order to facilitate the interpretation, we will use the same nomenclature as FLP, as what regards the identification of different condensations in HH 29. We have added the designations HH 29e for the emission knot SW of HH 29a, and HH 29f for the small emission 'knot' following HH 29 'proper' in hour angle (see Fig. 1).

The reduction was performed utilizing the ESO MIDAS package (ver. 92NOV and 95NOV) and the context ECHELLE and proceeded in a standard fashion.

The instrument profile was determined from Th-Ar comparison lines. From an analysis of 8 – 9 lines in each of three Th-Ar spectra obtained during both nights, we find the average full width at zero intensity of the instrument profile, FWZI$_I$ to be 43.3$\pm$ 4.8 km s^{-1}.

Flux calibration was achieved by observing HD74721 (Davis Philips & Hayes, 1983) on the first night and HR 718 (Hamuy et al. , 1992) on the second night. Standard extinction coefficients were extrapolated from data found on the ESO web site, taking into account also the anomalous atmospheric extinction introduced by the Mount Pinatoubo volcanic eruption. We

Table 2. FWZI of each knot in Hα. Ratios of high excitation and low excitation lines to Balmer lines

Feature	FWZI [1] km s^{-1}	[OII]/Hβ FLP[2]	[$OIII$]/Hβ FLP[2]	[OI]/Hα FLP[2]	[NII]/Hα This paper	[SII]/Hα This paper	[$CaII$]/Hα This paper
a	240	1.6	0.5	0.35	0.22	0.43	0.06
b	220	2.9	0.6	0.70	0.25	1.3	0.06
c	245	2.6	0.7	0.50	0.23	0.9	0.09
d	240	2.8	0.6	0.62	0.15	0.4	0.05
e	230	1.0	0.4	0.20	0.19	0.3	-
f	150	0.4	-	0.10	-	0.10	-

[1] Maximum FWZI$_M$ line width of Hα as defined in Sect. 3.1 for each knot
[2] Data from Fridlund, Liseau, Perryman (1993)

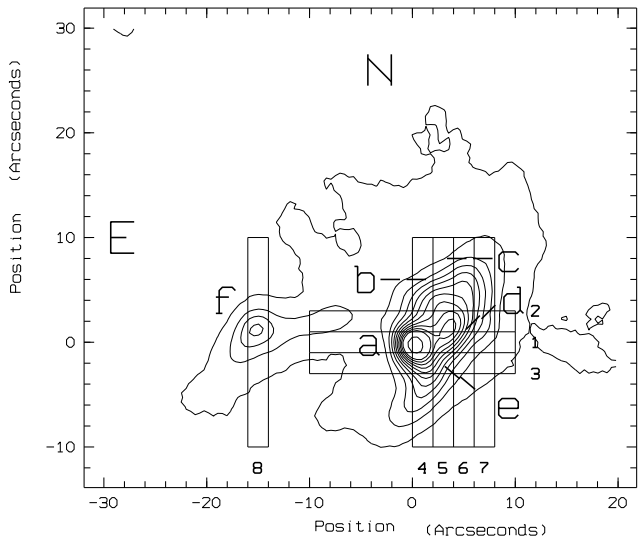

Fig. 1. The slit orientations and sizes used in our observations are shown superposed onto (part of) an Hα-band CCD image obtained with the ESO 3.5 m NTT (New Technology Telescope). The features a, b, c and d (FLP) are indicated as well as the new designations HH 29e & HH 29f introduced in this paper.

have compared our flux calibration with the results of FLP, and it is found that the level of accuracy for Hα, [SII] and [OI] is of the order of 10 %. The results from the second night are not quite as good, but since some of the same areas of HH 29 are covered on both nights, an internal adjustment leads to the same level of accuracy. One have also to take into account the probable variability of the object (LHFC). Our observations reported in this paper was however, carried out within a few months of the relevant imaging observations reported in FLP.

3. Results

3.1. Velocity structure

In Figs. 2, 3 and 4, we present examples of our data, clearly showing the quality of the observations.

The lines are broad and show a very complex structure both with respect to position and velocity. Referring now to Fig. 1 and Fig. 2, both of which displays Hα emission, attention is immediately drawn to a few features. In slits 1, 2 & 3 which pass through HH 29a, and immediately N and S of this knot, we see that the intensity gradient is steeper in the direction of IRS5, thus suggesting that the shock is located on this side. We also see, eastward of HH 29 'proper' (compare with Fig. 1), two fainter and well separated components. They have velocities of $\sim$ -130 km s^{-1}and -15 km s^{-1}(barycentric). It is conceivable that this emission could be due to recombination from a precursor to the shock, such as has been detected in HH34 by Heathcote & Reipurth (1992). The lower velocity component is found essentially at rest with respect to the telescope (and the molecular cloud L1551 within which HH 29 is located, V$_{LSR}$ =+7 km s^{-1}). Although usually not present, atmospheric Hα emission has been observed previously (L. Pasquini, private communication). It can thus not be excluded that part of this feature is caused by emission in the atmosphere of the Earth. Its structure can be discerned from Fig. 2 (slits 1, 2 & 3). The FWHM of this feature is, however, 1 pixel ($\sim$ 4.5 km s^{-1}) **wider** than the atmospheric lines of equivalent brightness found within the same and adjacent orders of the Echelle spectrogram. The brightness of the low velocity feature, also varies as a function of position along the slit. If we also refer to the last two panels in Fig. 2 (both corresponding to slit 8), it can be seen that the velocity of what we above called the -15 km s^{-1} component varies with an amplitude of several tens of km s^{-1} along the N-S direction of this slit. Taken together, all this indicates that at least some – if not most or all – of the emission is intrinsic to the region surrounding HH 29, although we can not *exclude* that part of the emission is of telluric origin. For the purposes of this paper we have taken all emission above the faintest level detected in this feature to be intrinsic. In Fig. 2 we have marked at what position in the structure this level is to be taken.

With regard to the component found at -130 km s^{-1} , comparison with Fig. 1 show that slits 1, 2 & 3 will admit emission from the feature HH 29f (compare slit 8 – two last panels of Fig. 2) at the spatial coordinates in question. We also see that the amount of Hα emission that is actually observed in the various slits is consistent with the faint high velocity component (the -130 km s^{-1} component) is being dominated by emission from HH 29f.

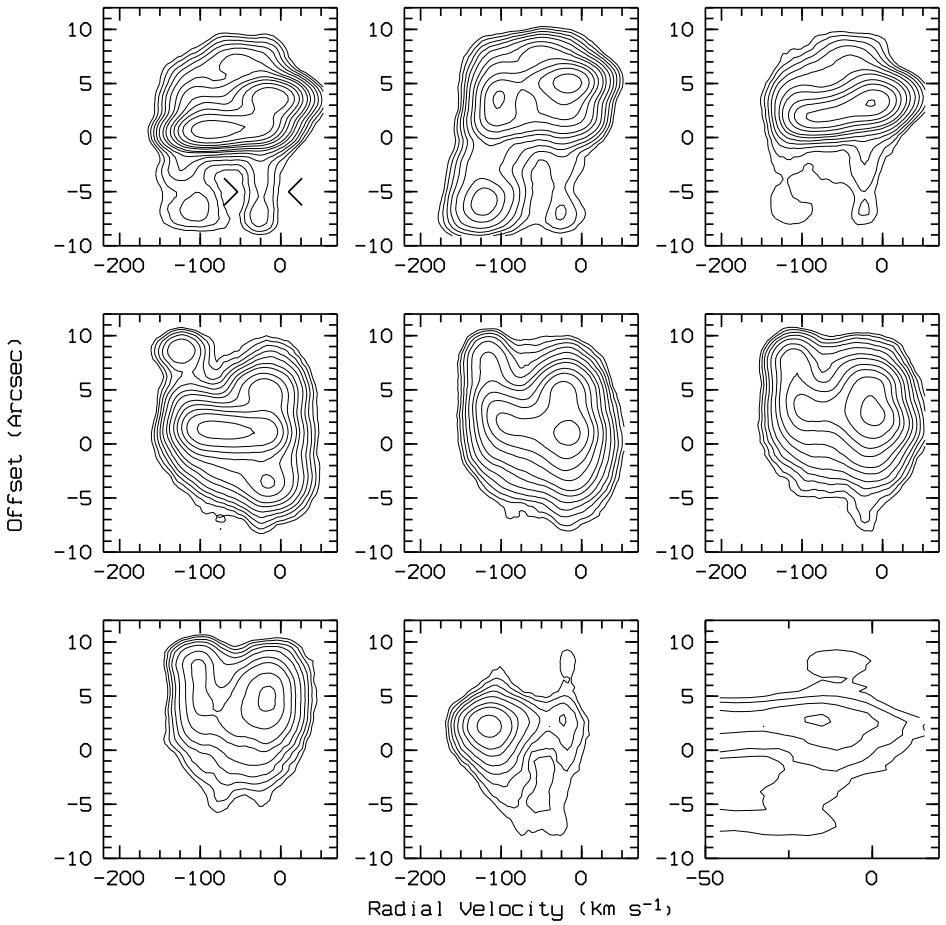

Fig. 2. Position velocity plots of the Hα spectra. They are: Top row – slits 1, 2 and 3; Middle row – slits 4, 5 and 6; Bottom row – slits 7, 8 and 8 shown at a different scale. We refer to Fig. 1 for the slit orientation. The velocity scale is barycentric. East is towards the bottom in the top row, while South is down in the rest of the panels. The lowest contour is 5 times the rms noise and each successive step is a factor $2^{\frac{1}{2}}$. The last panel displays the spectrum obtained through slit 8 on an expanded velocity scale. The upper left panel (slit 1) has the position marked where we have determined the *maximum* level of a possible atmospheric Hα contribution

Table 3. Observed Hα line fluxes. Units of 10^{-15} erg cm^{-2} s^{-1}

Position / Slit:	1	2	3	4	5	6	7	8
-8″,-6″	-	-	-	1.9	1.3	0.8	0.5	-
-6″,-4″	1.7	4.0	1.2	7.5	4.5	1.7	0.8	0.9
-4″,-2″	1.8	2.7	1.2	9.5	8.3	3.6	1.5	1.2
-2″,0″	15.3	4.4	2.4	19.6	17.8	9.4	3.4	2.8
0″,+2″	39.0	13.5	14.2	39.9	25.7	18.8	7.0	6.0
+2″,+4″	21.0	15.7	18.7	18.1	18.1	20.2	8.9	5.7
+4″,+6″	15.4	23.7	10.8	12.3	16.0	19.4	11.2	2.4
+6″,+8″	4.3	10.6	3.0	5.0	7.3	10.5	7.9	0.6
+8″,+10″	2.2	4.9	1.9	3.2	3.9	6.1	5.8	-
Background[1]	0.2	0.2	0.3	0.5	0.1	0.2	-0.1	0.1

[1] RMS value of the residual measured in the vicinity of the spectral line in question on the final science frames

The full line width at zero intensity, FWZI$_S$, corrected for the instrumental profile can be calculated according to $FWZI_S = \sqrt{(FWZI)^2_M - (FWZI)^2_I}$, which corresponds to the analytical solution of the deconvolution integral for Gaussian line profiles. Since a simple inspection of our data tells us that the profiles are *not* Gaussian, we have investigated how great a discrepancy is introduced if a simple measurement of at what velocity the line intensity goes to zero is performed instead. The discrepancy is found to be $\leq$ a few % and consequently we will use the FWZI$_M$ in the following.

In Table 1 we have listed the FWZI$_M$ of the detected lines at the position of HH 29a, and in Table 2 we list the same quantity for Hα for the other knots identified in HH 29.

We can use our high spectral resolution data in order to compare, qualitatively, with the models of HRH. In Fig. 3, we have displayed the full line profiles of the Hα line, over an area 7″ by 6″, centered on the (0″,0″) coordinate in Figs. 1, i.e. on

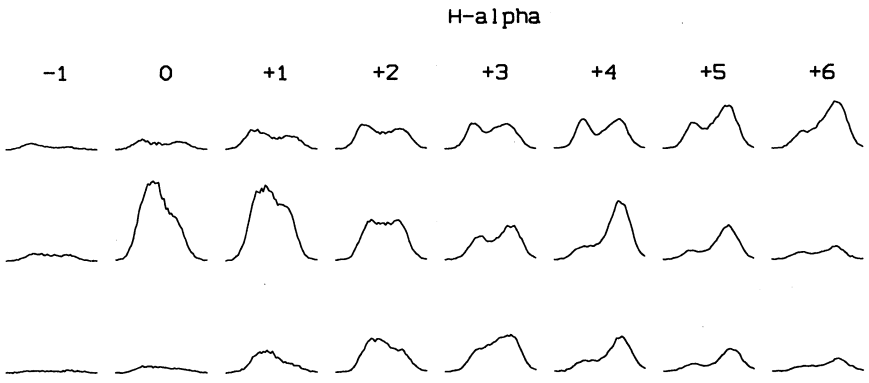

Fig. 3. The full Hα profiles from the a component of HH 29. The top row is from slit 2 followed in succession downwards by slits 1 and 3 (see Fig. 1). The scale in the EW direction is in arc seconds and indicated on the top. The resolution is thus $1''\times 2''$(corresponding to 140AU $\times$ 280AU). IRS5 is located $\sim$2.′3 towards the upper left (NE). The sudden onset of the shock is obvious, as is the radical change in the profiles over small spatial elements

the intensity maximum of the HH 29a component. Inspection of Fig. 3 and comparison with the Fig. 1 and the figures in FLP, show immediately the steep gradients in the profiles associated with features a & d respectively on opposite sides of the object. The line profiles of these two features, located $2''$ or less than 300AU apart, have the same FWZI$_M$, while the peak emission is separated by $\sim$ 90 km s^{-1}.

3.2. Line fluxes and line ratios

Following Raga et al. (1996), we have formed the line ratio [NII]6584Å/Hα for tracing high excitation conditions, and the ratios [OI]6300Å/Hα, [SII]$_{\Sigma 6717+6731}$/Hα and [CaII]7291Å/Hα - all of which trace zones of low level excitation. Further, we have taken the [OII]$_{\Sigma 3727+3729}$/Hβ and the [OIII]5007Å/Hβ ratios from the results of FLP as indicators of levels of high excitation. The latter ratio is a tracer of very high excitation. Note that all these ratios are for practical purposes to be considered reddening independent. The effect of a standard reddening law on the [CaII]7291Å/Hα ratio (the most affected) is 20%, which for our purposes is unimportant. The result is shown in Table 2, where we present the ratios for the features HH 29a, b, c, d, e and f.

In Table 3 we present the integrated flux of the Hα line within $2''$ bins along the slits. In Table 4 we then display the [SII]/Hα as well as the 6717Å/6731Å ratios. Here the data is thus presented in $2''$ bins over all of HH 29 and not only for the distinct features as in Table 1 and Table 2. The former of these ratios is mapping out the level of excitation over the projected surface of HH 29, while the latter ratio is a good measure of the electron density, n$_e$.

Since we are aiming for a three dimensional representation of HH 29, we have calculated the flux in Hα and both of the [SII] lines as a function of velocity, in 20 km s^{-1} bins, and also spatially in steps of $1''$ along the $2''$ wide slit. Selected parts of this data is presented in Table form and interpreted in Sect. 5.

4. Discussion

4.1. Shock structure

4.1.1. HH 29

In HH 29a, the steepest intensity gradient (indicating the location of the shock front or the apex of the bow shock) is found on the side *towards or closer to* the originating source, IRS5. The same is found upon close inspection of features HH 29b & (very clearly) HH 29f and – to some extent – for feature HH 29c. This is what would be expected from a 'shocked cloudlet' (Schwartz, 1978) and is indicative of a thinner, higher velocity, wind acting on denser, lower velocity material. Comparing Figs. 1, 2 and 3 we see that the opposite is true for feature HH 29d, where the steepest gradient is found on the side of the object *furthest away* from IRS5. This is more what would would be expected from an 'interstellar bullet' (Norman & Silk, 1979), or from a denser wind interacting with a thinner, slower moving medium (Hartigan, 1989). Interpreting our result qualitatively in terms of these models, we can then hypothesize that HH 29 is best explained as an aggregate of density enhancements in the wind traveling outwards into the ambient medium. It interacts with the (thinner) medium that it is plowing into, and this causes the shock feature HH 29d on the side of HH 29 *away* from IRS5 (the originating source). At the same time HH 29 is overtaken by a thin, faster wind component (possibly identical to the atomic component permeating the outflow lobe cavity – see Giovanardi et al. 1992), which causes the shocks at the position of features HH 29a, HH 29f and HH 29b to have the appearance of 'shocked cloudlets', i.e. with the shocks steepest gradient on the side of the feature *towards* IRS5. Inspection of the Hαline profiles displayed in Fig. 3 at the positions of HH 29a and HH 29d show that they are entirely consistent with this scenario.

The shock in HH 29a has a velocity of $\sim$ 90 km s^{-1} as determined by flux ratios (FLP utilizing the models of HRH). This is significantly slower than the velocity of HH 29 found from proper motions, $\sim$ 150 km s^{-1}(Cudworth & Herbig, 1979), the $\sim$ 190 km s^{-1}derived from the line profile of Hα by Stocke et al. (1988), or the FWZI (240 km s^{-1}) of Hα , at the position of HH 29a, given in this paper. The latter two results are thus indicative of shock velocities more than a factor 2 higher than what is derived from the flux ratios (using the same models of HRH where it is inherently assumed that width of the full line

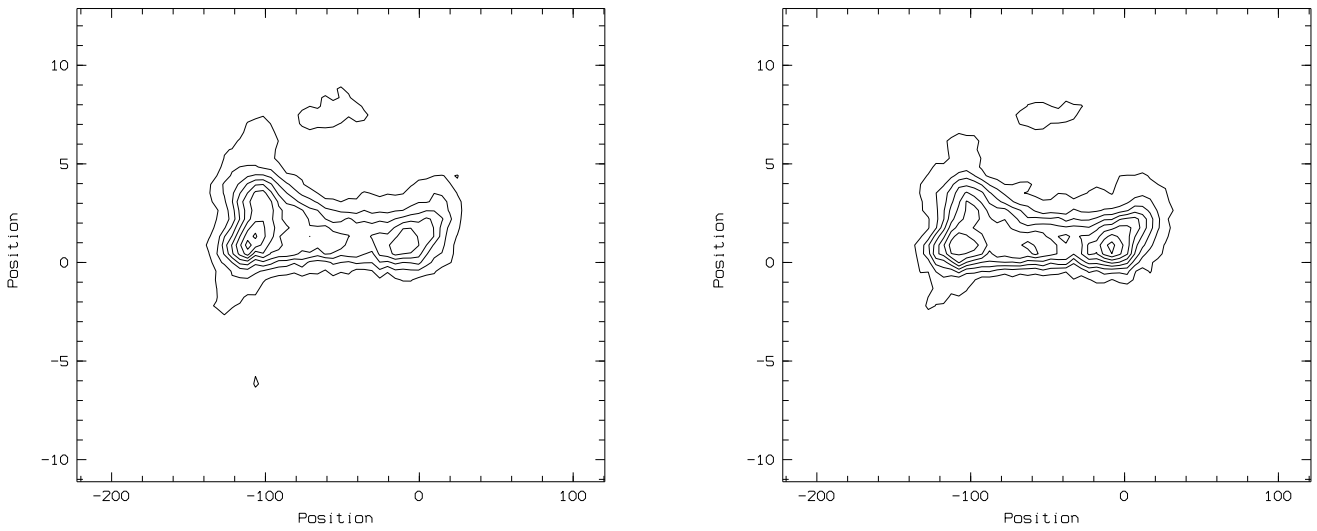

Fig. 4. Position velocity plots of the [SII] 6717Å (left) & 6731Å (right) spectra obtained through slit 1. The contours orientation and scales etc as in each panel of Fig. 2.

Table 4. The ratios of the sum of the 6717,6731Å lines to the Hα line (designated R_1) as well as the 6717/6731 ratio (designated R_2)

Position/Slit	1		2		3		4		5		6		7	
Ratios:	R_1	R_2	R_1	R_2	R_1	R_2	R_1	R_2	R_1	R_2	R_1	R_2	R_1	R_2
-4″,-2″	-	-	-	-	-	-	0.2(?)	1.1	0.1(?)	0.9	-	-	-	-
-2″,0″	0.3	0.8	0.4	1.2	-	-	0.3	1.0	0.3	1.1	0.2	1.2	0.2	1.2
0″,+2″	0.4	0.8	0.5	0.9	0.4	0.9	0.4	0.9	0.4	1.0	0.3	1.1	0.4	1.3
+2″,+4″	0.4	1.0	0.7	1.0	0.4	1.0	0.6	1.1	0.6	1.2	0.5	1.2	0.5	1.3
+4″,+6″	0.2	1.2	0.5	1.1	0.3	1.1	0.9	1.0	0.9	1.1	0.7	1.2	0.6	1.2
+6″,+8″	0.5	1.1	0.5	1.1	-	-	1.3	1.1	1.1	1.2	1.0	1.2	0.8	1.3
+8″,+10″	0.7	1.2	0.7	1.2	-	-	1.1	1.3	1.1	1.6	1.1	1.4	1.0	1.5

profile is equivalent to the shock velocity at the apex of the shock). The discrepancy between the V_S determined from line flux ratios and that determined from spectral profiles is a common phenomenon when interpreting data of this nature in the context of bow shock models, and has hitherto not received an adequate explanation (e.g. Böhm, 1995). Comparing the data in Tables 4 and 6, we see that although the integral flux ratio Hα/$\Sigma_{6717+6731}$[SII] for HH 29a is $\sim$ 2.5, when we look at the same ratio as a function of velocity it varies between 1 and 6, and this suggests one possible explanation.

4.1.2. Knot HH 29f and the two narrow components

Following the arguments in Sect. 3.1, we assume that the low velocity component (-15 km s^{-1}) is (mostly) intrinsic to the object. It is found at the rest velocity of the molecular cloud L1551, and this suggests that it is due to recombination in a precursor to the bright shock in HH 29a. Since this component is quite faint in our data the level of excitation and electron density can only be estimated from an individual inspection of the [SII] and Hα spectra. We find values of n_e ranging from 10 cm^{-3} to 300 cm^{-3}. The level of excitation in the -15 km s^{-1} component is as high as 0.3, as defined by the ratio between $[SII]_{6717+6731}$ to Hα.

As what concerns the high velocity component, we find from both the morphological appearance (compare Fig. 1 and Fig. 2) and from its velocity structure that it is most likely due to emission from the 'bridge' between HH 29a and the separate knot we have designated HH 29f. As mentioned above, inspection of the Hα spectrum obtained through slit 8 show the steepest gradient to appear also in this case on the side facing towards IRS5. HH 29f thus appears as a case of a 'shocked cloudlet'. The FWZI of the Hα profile at knot f is 150 km s^{-1}. In the region between HH 29a and HH 29f, we find n_e to be $\sim$ a few hundreds cm^{-3}.

4.2. Excitation and ionization

For a first determination of the excitation conditions, we can use the results of FLP. Table 2 shows the values of the [OIII]/Hβ and the [SII]6717Å+6731Å/Hα ratios. Comparing these values with the compilation of Raga et al. (1996) of $\sim$ 45 HH condensations, we find that HH 29 is one of the highest excitation Herbig Haro objects. This is also true individually for the a – d knots. HH 29b & c have unusual high

[SII]6717Å+6731Å/Hα ratio of 1.3 & 0.9 respectively given the [OIII]/Hβ value of 0.6 & 0.7 where the former show more of low excitation character. Strong [SII] relative to Hα is usually taken as an indication of low excitation shocks (see the Introduction), but is rarely found in combination with high values of [OIII]. We take this to indicate a combination of excitation conditions along the line of sight to the HH 29b & HH 29c features. The relatively strong [CaII] emission from the region of features b & c is consistent with this. Displaying the [SII]6717Å+6731Å/Hα ratio as a function of velocity (see below) confirms this hypothesis and show varying excitation conditions over velocity dispersions of $\sim$ 30 km s^{-1} – 50 km s^{-1}.

The present results alone do not allow a determination of T_e, but we can try to estimate it from the ratio of the [OII] 3726Å+3729Å flux (taken from FLP) to the 7318Å+7319Å+7330Å+7331Å flux. The blend between the red [OII] lines and [CaII] at 7323.88Å can be 'untangled' because of our high spectral resolution. A check of this procedure is allowed by a comparison between the theoretical and the measured value of the [CaII]7323.88Å to [CaII]7291Å ratio which should be equal to 0.67 (Brugel et al. , 1981). This is indeed the case (within our errors). Now, taking the UV-lines of [OII] fluxes from FLP, we find results (depending on the reddening applied to the UV-lines) of 5000K $\lesssim T_e \lesssim$ 7500K (Aller, 1984). In the paper of LHFC, we have shown HH 29 to be variable on time scales of less than 6 months in the satellite UV, however, and the range of T_e derived here can only be considered meaningful as an indication.

4.3. Hα flux, the level of excitation and the electron density, n_e, in a three dimensional representation

Based on the hypothesis that the emission is optically thin, the velocity profile of the lines in question contain information about the third dimension, i.e. along the line of sight. In this paper, we have determined the flux of Hα and the [SII]6717Å,6731Å lines in 20 km s^{-1} $\times$ 1″ $\times$ 2″ (the slit width) bins. Data for one of the slits (No. 1) is presented in table form in Tables 5, 6 & 7. F(Hα) is a representation of the emission measure, albeit with the proviso that we can have departures from a pure case B recombination spectrum in regions of weak shock conditions. As a first approximation, we can assume that case B is valid where we either have (relatively) strong [OIII]5007Å emission (from FLP) or high excitation/ionization conditions as determined by the H$\alpha/\Sigma_{6717+6731}$[SII] ratio. This ratio is the second parameter that we have determined from our data. Finally, the $[SII]_{6717}/[SII]_{6731}$ ratio is given as a measure of n_e.

We again see a structure where the physical conditions (as defined by these three quantities) change very rapidly. The highest value of n_e (as defined by low values of the $[SII]_{6717}/[SII]_{6731}$ ratio) is found at $\sim$ -50 to -90 km s^{-1}for knots a and d. The highest level of excitation (as defined by the H$\alpha/\Sigma_{6717+6731}$[SII] ratio) for knot a & b is also found within this velocity band while lower levels are found both at more negative and more positive velocities. Knot d, however, have its highest level of excitation at velocities between +10 km s^{-1} and -50 km s^{-1}. For knot b, the highest values of n_e is found between -10 km s^{-1} and -50 km s^{-1}. This all very strongly indicates that the 'clumps' are small structures.

The electron densities are derived by using a model for the 6717Å/[SII]6731Å ratio that incorporates 5 levels, Einstein A coefficients from Keenan et al. (1993) and new collisional coefficients calculated by Ramsbottom et al. (1996). This model was calculated for 3000K $\leq T_e \leq 10^5$K and for 1 cm^{-3} $\leq n_e \leq 10^{10}$ cm^{-3}.

Maps of the density as a function of velocity were created by integrating the line intensities (in arbitrary units) over velocity intervals of 10 km s^{-1}. Then the ratio of the 6717Å to the 6731Å was taken and the above mentioned density model for a fixed temperature of 10^4K was applied. A 2-dimensional cubic spline was then applied to each map which decreased the spatial resolution by a factor of 3. The maximum density at the position of HH 29a is $\sim 10^4$ cm^{-3}. Since this is the maximum density measurable with this method, this does not exclude higher values at this position. The value of n_e drops rapidly to lower values behind HH 29a, so that 3″ further 'downstream' from the intensity maximum we find densities of $\sim$ 500 cm^{-3}. The general structure of HH 29 appears very 'clumpy', with *smoothed* size scales of typicaly 2″ – 4″ (corresponding to $\sim$300 – 600 AU). The average density is also $\sim$ 300 cm^{-3}, with the density enhancements going well above several $\times$ 10^3 cm^{-3} for positions *near* features b,c,d and e. At these positions themselves, as defined by FLP, we find lower densities, however. The appearence of these 'clumps' is morphologically very similar to the A_V map of FLP, where density enhancements of several magnitudes where found with the same size scales. A comparison between Fig. 3 of FLP and our data shows the A_V enhancements to be *well offset* (i.e. more than 3″ – 4″) from the peak n_e 'clumps'.

The values of n_e are also velocity dependent, (as can be clearly seen from e.g. Table 7 so that the most extreme positive and particularly negative radial velocities ($\lesssim$ -100 km s^{-1}), are represented by *low* values of n_e.

A clumpy structure with n_e varying between $\sim$ 300 cm^{-3} and 10^4 cm^{-3} in the peak of the densest clump is thus indicated. Structures found in HST imaging of the L1551 IRS5 jet (HH154) (Fridlund et al. , 1997a & 1997b) are an order of magnitude smaller than what is resolved in the ground based observations, and our calculation above can not exclude structural variations on such a small scale also being present in HH 29. On the contrary, the time series UV data of LHFC strongly suggests even smaller spatial scale structures being present. Nevertheless, our observations indicate a large filling factor whether originating in (relatively) large structures or in agglomerates of smaller structures. When we analyze the [SII]6717/6731 ratios as a function of velocity, we see large variations on scales as small as a few $\times$ 10 km s^{-1}. We take also this to be a suggestion of small (spatial) scale structural variations along the line of sight.

Table 5. Observed line fluxes in the Hα line along slit 1 at 1″ intervals. The flux is integrated in 1″ × 2″ bins. Units of 10^{-15} erg cm^{-2} s^{-1}

Vel/Pos:	-4”	-3”	-2”	-1”	0”	+1”	+2”	+3”	+4”	+5”	+6”	+7”
-230	-0.02	-0.02	-0.02	-0.01	-0.02	-0.02	-0.03	-0.02	-0.02	-0.03	-0.02	-0.02
-210	0.00	0.01	0.00	0.00	0.01	0.01	-0.01	0.00	0.00	0.00	0.00	0.00
-190	0.01	0.01	0.00	0.01	0.04	0.02	0.01	0.02	0.00	0.01	0.02	0.02
-170	0.06	0.05	0.05	0.07	0.16	0.12	0.08	0.06	0.06	0.06	0.05	0.05
-150	0.14	0.14	0.17	0.32	0.76	0.64	0.35	0.25	0.24	0.20	0.12	0.08
-130	0.19	0.24	0.34	0.85	2.26	2.07	1.26	0.65	0.60	0.54	0.26	0.15
-110	0.14	0.17	0.37	1.37	3.93	3.90	2.54	1.12	0.84	0.75	0.40	0.27
-90	0.08	0.10	0.32	1.45	4.51	4.55	3.15	1.28	0.88	0.68	0.43	0.40
-70	0.06	0.08	0.29	1.18	4.09	4.41	2.92	1.13	0.95	0.74	0.41	0.52
-50	0.06	0.08	0.28	0.96	3.25	3.82	2.87	1.40	1.49	1.17	0.45	0.58
-30	0.14	0.15	0.33	0.85	2.79	3.52	3.08	2.09	2.51	1.91	0.56	0.52
-10	0.16	0.15	0.33	0.73	2.18	3.02	3.24	2.76	3.41	2.49	0.62	0.42
10	0.07	0.08	0.19	0.39	1.06	1.61	2.32	2.63	3.12	2.04	0.39	0.20
30	0.03	0.04	0.07	0.13	0.33	0.50	1.01	1.53	1.80	1.10	0.16	0.07
50	0.01	0.00	0.02	0.02	0.08	0.12	0.29	0.49	0.57	0.34	0.05	0.02
70	0.00	0.00	0.01	0.02	0.03	0.03	0.08	0.12	0.15	0.08	0.00	0.00

Table 6. Observed level of excitation along slit 1 at 1″ intervals. The flux was integrated in 1″ × 2″ bins. The level of excitation is defined as the ratio of Hα to [SII]

Vel./Pos:	-4”	-3”	-2”	-1”	0”	+1”	+2”	+3”	+4”	+5”	+6”	+7”
-150	0.00	0.00	0.00	0.00	0.00	0.00	0.00	0.00	0.00	0.00	0.00	0.00
-130	0.00	1.50	1.01	2.70	3.89	2.73	2.06	1.46	1.45	1.71	2.03	0.00
-110	1.26	1.45	1.17	2.66	3.03	1.96	1.13	0.77	0.81	1.15	1.15	1.27
-90	0.00	0.00	3.18	5.34	4.33	2.70	1.42	0.94	1.11	1.63	1.70	1.80
-70	0.00	0.00	0.00	5.89	4.54	2.88	1.73	1.71	3.34	4.20	2.66	1.76
-50	0.00	0.00	0.00	4.77	3.84	2.71	2.12	3.75	8.16	8.03	3.48	1.78
-30	0.00	0.00	0.00	3.69	3.21	2.56	2.35	5.13	10.30	9.69	0.00	2.80
-10	0.00	0.00	3.39	2.11	1.87	1.67	1.93	5.64	11.65	13.38	0.00	0.00
10	0.00	0.00	0.00	1.78	1.80	1.63	1.63	4.08	8.20	9.43	0.00	0.00
30	0.00	0.00	0.00	0.00	2.85	2.46	2.91	5.99	9.80	9.69	0.00	0.00

Table 7. Observed ratio of the [SII] lines along slit 1 at 1″ intervals. The flux was integrated in 1″ × 2″ bins.

Vel/Pos:	-4”	-3”	-2”	-1”	0”	+1”	+2”	+3”	+4”	+5”	+6”	+7”
-150	0.00	0.00	0.00	0.00	0.00	0.00	0.00	0.00	0.00	0.00	0.00	0.00
-130	0.00	1.31	1.12	0.93	0.74	0.78	0.84	0.92	1.10	1.30	1.29	0.00
-110	1.18	1.22	1.28	1.02	0.86	0.96	1.03	1.13	1.26	1.39	1.29	1.64
-90	0.00	0.00	1.38	0.96	0.80	0.90	1.03	1.19	1.43	1.51	1.34	1.30
-70	0.00	0.00	0.00	0.92	0.63	0.77	0.97	1.19	1.09	1.16	0.75	1.01
-50	0.00	0.00	0.00	0.73	0.66	0.76	0.89	1.04	0.93	1.18	0.86	0.88
-30	0.00	0.00	0.00	0.65	0.69	0.75	0.84	0.94	1.09	1.07	0.00	1.15
-10	0.00	0.00	1.39	0.75	0.69	0.74	0.79	0.95	0.90	0.90	0.00	0.00
10	0.00	0.00	0.00	0.92	0.90	0.87	0.84	0.96	1.04	0.93	0.00	0.00
30	0.00	0.00	0.00	0.00	0.86	0.86	0.84	0.96	1.14	1.46	0.00	0.00

5. Conclusions

Our main conclusions from this work can briefly be summarized as follows:

1. A 3D map (velocity being the third dimension) of the Hα-flux, the level of excitation and the n_e have been derived. The strucure is very ‘clumpy’ with densities going up to 10^4 cm^{-3} (maximum detectable with this method) and with spatial scales equal or smaller than the resolution $\sim 2''$. The clump dispersion in velocity is of the order of 30 km s^{-1} to 50 km s^{-1}. The clumps are found immersed in an ‘inter-clump medium’ with $n_e \sim 10$ cm^{-3} – 300 cm^{-3}.
2. In HH 29 one can identify at least 6 separate features. Knots a – f are all well defined both morphologically and spectroscopically.

3. Knots a, d, & e have a clear high excitation character while b & c are of the low excitation variety as derived from the [SII]/Hα ratio. Nevertheless, these two latter features have a relatively high value of their [OIII]/Hβ ratio, indicating high excitation characteristics along the line-of-sight towards these objects. This is also strongly indicated by the change of n_e and level of excitation with velocity.
4. The 'clump' with the highest n_e and the largest F(Hα) is HH 29a. The highest level of excitation is found in HH 29d.
5. Both the high excitation knots and the low excitation knots have FWZI of $\sim$ 230 km s^{-1} in Hα. The peak velocity of the brightest peak varies for each of the features.
6. The spectral characteristics and the position of the shock gradient with respect to the originating source for knots a, b, possibly c & f suggests them to be best explained by models of the 'shocked cloudlet' type, i.e. a thinner faster wind that interacts with slower more dense material further out from the originating source. The observations of feature d instead indicates the opposite, i.e. denser material overtaking a thinner medium.
7. A model based on these facts and which is consistent with the known characteristics of L1551 IRS5 including the structure of the L1551 molecular outflow, suggests HH 29 to be an aggreagate of denser clumps in the outflow plowing into either ambient material or a slower less dense wind component (perhaps older – IRS5 is known to have FU Orionis characteristics), at the same time being overtaken by a faster (thinner) wind.

Acknowledgements. We wish to express our gratitude to the ESO staff at La Silla. We also appreciate the support this project has received by Miss Monica Huldtgren. RL thanks the Swedish National Space Board for financially supporting the project. We also wish to acknowledge the report of an anonymous referee whose comments resulted in a stricter paper

References

Aller L.H., 1984, Physics of thermal gaseous nebulae, D. Reidel Publishing Company, Dordrecht/Boston/Lancaster
Brugel E.W., Böhm K.H., Mannery E., 1981, ApJS 47, 117
Böhm K-H, 1995, Ap&SS 233, 11
Cameron M., Liseau R., 1990, A&A 240, 409
Canto J., 1980, A&A 86, 327
Choe, S-U., Böhm K-H, Solf, J., 1985., ApJ 288, 338
Cudworth K.M., Herbig G.H., 1979, AJ 84, 548
Davis Philip A.G., Hayes D.S., 1983, ApJS 53, 751
Elias J., 1978 ApJ 224, 857
Fridlund C.V.M., Liseau R.,1994, A&A 292, 631
Fridlund C.V.M., Nordh H.L., van Duinen R.J., Aalders J.W.G., Sargent A.I., 1980, A&A 91, L1
Fridlund C.V.M., Liseau R., Perryman M.A.C., 1993, A&A 273, 601 (FLP)
Fridlund C.V.M., Huldtgren M., Liseau R., 1997a, in Reipurth B. and Bertout C. (eds) Herbig-Haro flows and the birth of low mass stars, IAU symposium No. 182, Kluwer Academic Publishers, p. 19
Fridlund C.V.M., Liseau R., Huldtgren M., 1997b, in prep.
Giovanardi C., Lizano S., Natta A., Evans N.E., Heiles C., 1992, ApJ 397, 214
Hamuy M., Walker A.R., Suntzeff N.B., Gigoux P., Heathcote S.R., Phillips M.M., 1992, PASP 104, 533
Hartigan P., 1989, ApJ 339, 987
Hartigan P., Raymond J., Hartmann L., 1987, ApJ 316, 323 (HRH)
Heathcote S., Reipurth B., 1992, AJ 104, 2193
Keenan et al. 1993, Phys. Scripta 48, 129
Königl A., 1982, ApJ 261, 115
Liseau R., Huldtgren M., Fridlund C.V.M., Cameron M., 1996, A&A 306, 255 (LHFC)
Mundt R., Fried J., 1983, ApJ 274, L83
Norman C.A., Silk J., 1979, ApJ 228, 197
Raga A.C., 1995, in: Lizano S. and Torelles J.M. (eds.) Circumstellar disks, outflows and star formation, Rev. Mex. Astron. Astrof. 1, 103
Raga A.C., Böhm K.-H., Cantó, 1996, Rev. Mex. Astron. Astrof. 32, 161
Ramsbottom C.A., Bell K.L., Stafford R.P., 1996, Atomic Data and Nuclear Data Tables 63, 57
Schwartz R.D., 1978, ApJ 223, 884
Staude H.J., Elsässer H., 1993, A&AR 5, 165
Stocke J.T., Hartigan P.M., Strom S.E., et al., 1988, ApJS 68, 229

This article was processed by the author using Springer-Verlag LaTeX A&A style file *L-AA* version 3.